BUCKLING OF STIFFENED COMPOSITE PANELS WITH STRINGER TERMINATIONS

Enzo Cosentino and Paul Weaver

BUCKLING OF STIFFENED COMPOSITE PANELS
WITH STRINGER TERMINATIONS

ENZO COSENTINO AND PAUL WEAVER

A meshless approach is developed and used to predict buckling of discretely assembled multibay composite panels made from skin and stiffeners. The effect of eccentricity is included in the formulation. Particular emphasis is given to stringer run-outs within a stiffened panel, where abrupt eccentricity can trigger very large transverse displacements of the skin in front of the run-out tip. The model is obtained by combining von Karman's formulation for moderately large deflections in plates with an extended Timoshenko approach for small initial perturbations. Solutions are calculated by means of a Rayleigh–Ritz approach in conjunction with a Galerkin technique. Hilbert's orthogonal eigenfunctions are employed to obtain a generalized Fourier series expansion of the variables of interest. Limits of applicability, convergence of results and further potential exploitations are discussed. Numerical results obtained are compared with finite element analysis.

A list of symbols can be found on page 1532.

1. Introduction

It is becoming increasingly important to make further weight savings with composite cocured/cobonded assemblies. With the new generation of integral composite assemblies, critical and sometimes unexpected failure modes are challenging the weight saving philosophy that is associated with the use of carbon fibre reinforced composites. A major advantage of composites is their inherent ability to tailor elastic properties for maximizing performance. A further advantage is that different components can be assembled together without making use of fasteners, since the load transfer can be achieved through the interlaminar shear stresses arising within the bond line of an adhesive. Unfortunately, laminated composites exhibit relatively poor response when the loads act perpendicular to the fibers' plane. The weakest areas are typically the bond lines. This weakness is sometimes exacerbated by the anisotropic response of laminated composites, which could trigger out-of-plane displacements when panels undergo loads that align with the fibers' plane. Hence, premature failure is likely to happen in the bond line due to disbond or delamination. This behavior is particularly critical in thick-sectioned composite laminates, where the induced through-the-thickness stresses are comparable in magnitude to the main in-plane stresses. The current level of confidence for the prediction of external loads that may cause delamination and/or disbond often precludes those phenomena, such as buckling, which might trigger significant out-of-plane displacements, leading to complex and potentially catastrophic failure modes. As a result, composite panels for aerospace applications are often designed to minimize or eliminate such failure modes, and to allow for redundant load paths, which are able to guarantee the fail safe requirements. "Chicken" fasteners are extensively used in the majority of primary aerospace composite structure, thwarting potential weight

---
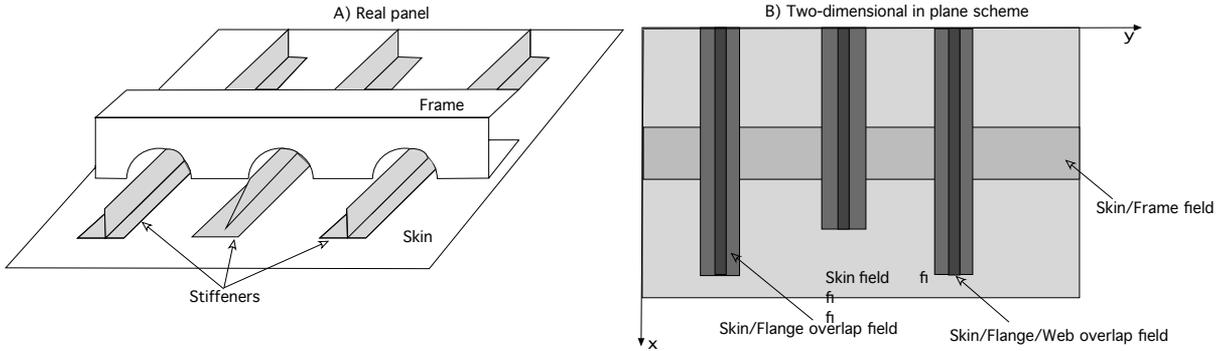
Figure 1. Example of the skin/stringers/frame multibay assembly. Left: realized structure; right: in-plane projections.

saving associated with an "integral" design. Also, as a general design principle (commonly accepted by many of the aerospace industries), the majority of thick-sectioned primary structures are designed not to buckle, thus penalizing the final weight. It is evident that a precise calculation of the buckling loads is vital in order to minimize the structural weight and reserve factors.

The present study is motivated by the need to develop a robust and reliable technique able to combine acceptable accuracy with low computational expense. It is intended to provide aerospace designers with a rapid method that can be used in the preliminary sizing phase, when the need for analyzing hundreds of load cases within restricted time scales, requires very low computational expenses.

2. Field equations

The purpose of the present study is to establish a fast, robust, and sufficiently accurate methodology to predict displacement and stress fields throughout the entire domain of composite skin/stiffeners assemblies in the prebuckling regime and then calculate buckling loads and mode shapes.

The buckling load calculation is done using the formulation developed in [Cosentino and Weaver 2008] with modified eigenfunctions [Cosentino and Weaver 2009] to improve the accuracy of the solution. Two different sets of eigenfunctions are employed to model the transverse displacement and the neutral plane, so providing a more accurate description of the internal loads distribution, particularly near boundaries. As a first approximation, a linear buckling analysis [Kollar and Springer 2003, Chapter 4], which neglects the effect of in-plane loads eccentricities, is proposed.

The use of von Karman nonlinear field equations allows a single variable, that is, the transverse deflection w, to be used. Following [Cosentino and Weaver 2008], the beam properties of the stiffeners are locally homogenized over the plate as represented in Figure 1, right (calculations are shown in Appendix A). The global domain is therefore partitioned into subdomains (fields).

The equivalent field properties are then smeared over the regions defined by the boundaries of the stiffeners' feet (areas in light gray in Figure 1). Abrupt discontinuities of the functions expressing the neutral plane (loads eccentricity) and the structural properties (that is, A, B, and D matrices) occur at the same boundaries.

Membrane strains and the curvatures are expressed as functions of the transverse displacement as follows:

$$\varepsilon_x^0 = \frac{\partial u_o}{\partial x} + \frac{1}{2}\left(\frac{\partial w}{\partial x}\right)^2, \qquad \varepsilon_{xy}^0 = \frac{\partial u_0}{\partial y} + \frac{\partial v_0}{\partial x} + \frac{\partial w}{\partial x}\frac{\partial w}{\partial y}, \qquad \varepsilon_y^0 = \frac{\partial v_0}{\partial y} + \frac{1}{2}\left(\frac{\partial w}{\partial y}\right)^2 \tag{1}$$

$$k_x = -\frac{\partial^2 w}{\partial x^2}, \qquad k_x = -\frac{\partial^2 w}{\partial y^2}, \qquad k_{xy} = -2\frac{\partial^2 w}{\partial x\,\partial y}. \tag{2}$$

The constitutive equations of the laminate expressed in the partially inverted form are [Jones 1975; Reddy 2004]

$$\begin{bmatrix} \boldsymbol{\varepsilon}^0 \\ \boldsymbol{M} \end{bmatrix} = \begin{bmatrix} \boldsymbol{A}^* & \boldsymbol{B}^* \\ -\boldsymbol{B}^{*T} & \boldsymbol{D}^* \end{bmatrix} \begin{bmatrix} \boldsymbol{N} \\ \boldsymbol{k} \end{bmatrix}, \tag{3}$$

where

$$\boldsymbol{\varepsilon}^0 = \begin{bmatrix} \varepsilon_x^0 \\ \varepsilon_y^0 \\ \varepsilon_{xy}^0 \end{bmatrix}, \qquad \boldsymbol{k} = \begin{bmatrix} k_x \\ k_y \\ k_{xy} \end{bmatrix}, \qquad \boldsymbol{N} = \begin{bmatrix} N_x \\ N_y \\ N_{xy} \end{bmatrix}, \qquad \boldsymbol{M} = \begin{bmatrix} M_x \\ M_y \\ M_{xy} \end{bmatrix}. \tag{4}$$

The rectangular panel sketched in Figure 1 is subjected to distributed external in-plane loads N_{x0}, N_{y0}, and N_{xy0} around the edges and to a transverse load $q(x, y)$ defined over the rectangular domain. Following, for example, [Mansfield 1989, pp. 85–90], the total strain energy U due to bending is

$$\begin{aligned}
U &= \frac{1}{2}\int_0^{l_x}\int_0^{l_y} \boldsymbol{k}^T \boldsymbol{M}\,dx\,dy = \frac{1}{2}\int_0^{l_x}\int_0^{l_y} \boldsymbol{k}^T \boldsymbol{D}^* \boldsymbol{k}\,dx\,dy \\
&= \frac{1}{2}\int_0^{l_x}\int_0^{l_y}\left[D_{11}^*\left(\frac{\partial^2 w}{\partial x^2}\right)^2 + D_{22}^*\left(\frac{\partial^2 w}{\partial y^2}\right)^2 + 4D_{66}^*\left(\frac{\partial^2 w}{\partial x\,\partial y}\right)^2 + 2D_{12}^*\frac{\partial^2 w}{\partial x^2}\frac{\partial^2 w}{\partial y^2} \right. \\
&\qquad\qquad\qquad \left. + 4D_{16}^*\frac{\partial^2 w}{\partial x^2}\frac{\partial^2 w}{\partial x\,\partial y} + 4D_{26}^*\frac{\partial^2 w}{\partial y^2}\frac{\partial^2 w}{\partial x\,\partial y}\right]dx\,dy.
\end{aligned} \tag{5}$$

The potential Ω_N of external in-plane forces is [Cosentino and Weaver 2008]

$$\Omega_{N,L} = \frac{1}{2}\int_0^{l_x}\int_0^{l_y}\left[N_x\left(\frac{\partial w}{\partial x} + \frac{\partial e}{\partial x}\right)^2 + N_y\left(\frac{\partial w}{\partial y} + \frac{\partial e}{\partial y}\right)^2 + 2N_{xy}\frac{\partial(w+e)}{\partial x}\frac{\partial(w+e)}{\partial y}\right]dx\,dy, \tag{6}$$

where $e(x, y)$ is the neutral plane function which is treated as a moderately large initial perturbation and expanded in generalized Fourier series by means of a Galerkin technique [Cosentino and Weaver 2008; 2009].

Similarly, the potential Ω_Q of the transverse load is [Cosentino and Weaver 2008]

$$\Omega_Q = -\int_0^{l_x}\int_0^{l_y} qw\,dx\,dy. \tag{7}$$

The total linear potential energy Π_L of the system is therefore

$$\Pi_L = U + \Omega_{N,L} + \Omega_Q. \tag{8}$$

In order to properly utilize the Rayleigh–Ritz method, approximate expressions for the unknown variables w and for the eccentricity e in generalized coordinates are required, which satisfy the geometric

boundary conditions. The following series expansions satisfy the above conditions:

$$w = \sum_{m=1}^{M_w} \sum_{n=1}^{N_w} w_{mn} X_m(x) Y_n(y), \qquad e = \sum_{m=1}^{M_w} \sum_{n=1}^{N_w} e_{mn} \bar{X}_m(x) \bar{Y}_n(y), \qquad (9)$$

where $X_m(x)$, $Y_n(y)$, $\bar{X}_m(x)$, and $\bar{Y}_n(y)$ are continuous and indefinitely differentiable functions. Wherever possible, it is recommended to use beam eigenfunctions that satisfy the orthogonality relations [Cosentino and Weaver 2008; 2009] for both the transverse displacement and the neutral plane function.

To simplify software implementation the following vectors use only one index:

$$\varphi = \begin{bmatrix} X_1 Y_1 & X_1 Y_2 & \cdots & X_1 Y_{N_w} & X_2 Y_1 & X_2 Y_2 & \cdots & X_2 Y_{N_w} & \cdots & X_{M_w} Y_1 X_{M_w} & Y_2 X_M Y_N \end{bmatrix}^T, \qquad (10)$$

$$\bar{\varphi} = \begin{bmatrix} \bar{X}_1 \bar{Y}_1 & \bar{X}_1 \bar{Y}_2 & \cdots & \bar{X}_1 \bar{Y}_{N_w} & \bar{X}_2 \bar{Y}_1 & \bar{X}_2 \bar{Y}_2 & \cdots & \bar{X}_2 \bar{Y}_{N_w} & \cdots \bar{X}_{M_w} & \bar{Y}_1 \bar{X}_{M_w} & \bar{Y}_2 \bar{X}_{M_w} & \bar{Y}_{N_w} \end{bmatrix}^T,$$

$$\boldsymbol{W} = \begin{bmatrix} w_1 & w_2 & \cdots & w_{M \times N} \end{bmatrix}^T, \qquad \boldsymbol{E} = \begin{bmatrix} e_1 & e_2 & \cdots & e_{M_w \times N_w} \end{bmatrix}^T. \qquad (11)$$

Equations (9) can, therefore, be rewritten, more simply, as

$$w = \sum_{i=1}^{M \times N} w_i \varphi_i(x, y), \qquad e = \sum_{j=1}^{M \times N} e_j \bar{\varphi}_j(x, y), \qquad (12)$$

where it is straightforward to show that the functions φ_i and $\bar{\varphi}_j$ satisfy the two-dimensional orthogonality relations

$$\int_0^{l_x} \int_0^{l_y} \varphi_p(x, y) \varphi_q(x) dx\, dy \begin{cases} = 0 & p \neq q \\ \neq 0 & p = p \end{cases}, \qquad \int_0^{l_x} \int_0^{l_y} \bar{\varphi}_l(x, y) \bar{\varphi}_m(x) dx\, dy \begin{cases} = 0 & l \neq m \\ \neq 0 & l = m \end{cases}. \qquad (13)$$

Equations (12), combined with the definition of beam eigenfunctions, guarantee that every function defined inside the considered domain and fulfilling the same essential boundary conditions as the panel and the neutral plane, can be expressed as a linear combination of such eigenfunctions.

If M and N are reasonably large integers, then the error induced when truncating the summation is negligible. Yet, generic functions defined with different boundary conditions inside the domain can be expressed as truncated linear combinations by means of a Galerkin technique. This technique is used in [Cosentino and Weaver 2008; 2009] to calculate the e_j in (12).

Expressing the neutral plane as a linear combination of basis functions allows differentiation of the total potential energy in a closed form, obtaining a final compact formulation, which is derived and expressed in (19) and that is also readily implemented in software.

Substituting (12) into (5), (6), and (7) the total potential is expressed as a second order polynomial of the $M \times N$ unknown coefficients w_i. The expressions for U, Ω_N, and Ω_Q are

$$U = \frac{1}{2} \int_0^{l_x} \int_0^{l_y} \sum_{i=1}^{M \times N} \sum_{j=1}^{M \times N} \Big(D_{11}^* \varphi_{,xx,i}\, \varphi_{,xx,j} + D_{22}^* \varphi_{,yy,i}\, \varphi_{,yy,j} + 4 D_{66}^* \varphi_{,xy,i}\, \varphi_{,xy,j}$$

$$+ 2 D_{12}^* \varphi_{,xx,i}\, \varphi_{,yy,j} + 4 D_{16}^* \varphi_{,xx,i}\, \varphi_{,xy,j} + 4 D_{26}^* \varphi_{,yy,i}\, \varphi_{,xy,j} \Big) w_i w_j\, dx\, dy, \qquad (14)$$

$$\Omega_Q = -\int_0^{l_x}\int_0^{l_y} q(x,y)\sum_{i=1}^{M\times N}\phi_i w_i\,dx\,dy, \tag{15}$$

$$\Omega_{N,L} = \frac{1}{2}\int_0^{l_x}\int_0^{l_y}\sum_{i=1}^{M\times N}\sum_{j=1}^{M\times N}\left(N_x\varphi_{,x,i}\,\varphi_{,x,j}+N_y\varphi_{,y,i}\,\varphi_{,y,j}+2N_{xy}\varphi_{,x,i}\,\varphi_{,y,j}\right)w_i w_j\,dx\,dy$$

$$+\frac{1}{2}\int_0^{l_x}\int_0^{l_y}\sum_{i=1}^{M\times N}\sum_{j=1}^{M\times N}\left(2N_x\varphi_{,x,i}\,\overline{\varphi}_{,x,j}+2N_y\varphi_{,y,i}\,\overline{\varphi}_{,y,j}+2N_{xy}(\varphi_{,x,i}\,\overline{\varphi}_{,y,j}+\varphi_{,y,i}\,\overline{\varphi}_{,x,j})\right)w_i e_j\,dx\,dy$$

$$+\frac{1}{2}\int_0^{l_x}\int_0^{l_y}\sum_{i=1}^{M\times N}\sum_{j=1}^{M\times N}\left(N_x\overline{\varphi}_{,x,i}\,\overline{\varphi}_{,x,j}+N_y\overline{\varphi}_{,y,i}\,\overline{\varphi}_{,y,j}+2N_{xy}\overline{\varphi}_{,x,i}\,\overline{\varphi}_{,y,j}\right)e_i e_j\,dx\,dy. \tag{16}$$

Using the principle of stationary potential energy [Cosentino and Weaver 2008; 2009], we have

$$\frac{\partial\Pi_L}{\partial w_i}=0,\quad \forall i=1,\ldots,M_w\times N_w. \tag{17}$$

Equations (14), (15), and (16) are now substituted into (17) with the result differentiated with respect to w_i. Algebraic manipulations result in the following linear system of $M\times N$ equations in the $M\times N$ unknowns $w_i,\,i=1,\ldots,N$:

$$(\boldsymbol{G}+\boldsymbol{H})\boldsymbol{W}=-\overline{\boldsymbol{H}}\boldsymbol{E}+\boldsymbol{Q}, \tag{18}$$

where the vectors $\boldsymbol{Q}$, $\boldsymbol{E}$ and the matrices $\boldsymbol{G}$, $\boldsymbol{H}$, $\overline{\boldsymbol{H}}$ are defined as

$$\boldsymbol{Q}_i = \int_0^{l_x}\int_0^{l_y} q\phi_i\,dx\,dy, \tag{19}$$

$$\boldsymbol{E}=[e_1\quad e_2\quad\cdots\quad e_{M\times N}]^T, \tag{20}$$

$$\boldsymbol{G}_{ij}=\frac{1}{2}\int_0^{l_x}\int_0^{l_y}\left[2D_{11}^*\varphi_{,xx,i}\,\varphi_{,xx,j}+2D_{22}^*\varphi_{,yy,i}\,\varphi_{,yy,j}+8D_{66}^*\varphi_{,xy,i}\,\varphi_{,xy,j}+2D_{12}^*(\varphi_{,xx,i}\,\varphi_{,yy,j}\right.$$

$$\left.+\varphi_{,xx,j}\,\varphi_{,yy,i})+4D_{16}^*(\varphi_{,xx,i}\,\varphi_{,xy,j}+\varphi_{,xx,j}\,\phi_{,xy,i})+4D_{26}^*(\varphi_{,yy,i}\,\varphi_{,xy,j}+\varphi_{,yy,j}\,\varphi_{,xy,i})\right]dx\,dy, \tag{21}$$

$$\boldsymbol{H}_{ij}=\frac{1}{2}\int_0^{l_x}\int_0^{l_y}\left[2N_x\varphi_{,x,i}\,\varphi_{,x,j}+2N_y\varphi_{,y,i}\,\varphi_{,y,j}+2N_{xy}(\varphi_{,x,i}\,\varphi_{,y,j}+\varphi_{,x,j}\,\varphi_{,y,i})\right]dx\,dy, \tag{22}$$

$$\overline{\boldsymbol{H}}_{ij}=\frac{1}{2}\int_0^{l_x}\int_0^{l_y}\left[2N_x\varphi_{,x,i}\,\overline{\varphi}_{,x,j}+2N_y\varphi_{,y,i}\,\overline{\varphi}_{,y,j}+2N_{xy}(\varphi_{,x,i}\,\overline{\varphi}_{,y,j}+\overline{\varphi}_{,x,j}\,\varphi_{,y,i})\right]dx\,dy. \tag{23}$$

For a linear buckling analysis, the external transverse load $q(x,y)$ and the effect of the neutral plane eccentricity are neglected. Only the magnitude of the in-plane loads is noteworthy for the onset of buckling. It is assumed that the presence of transverse loads and/or eccentricity only influences the deformed shape of the panel when the external load has reached the critical buckling level. The effect of eccentricity is formally equivalent to a localized transverse bending moment, which does not affect the membrane stretching in a linear calculation. The right-hand side of (18), the associated eigenvalues problem is expressed by

$$(\boldsymbol{H}^{-1}\boldsymbol{G}+\lambda\boldsymbol{I})\boldsymbol{W}=\boldsymbol{0}, \tag{24}$$
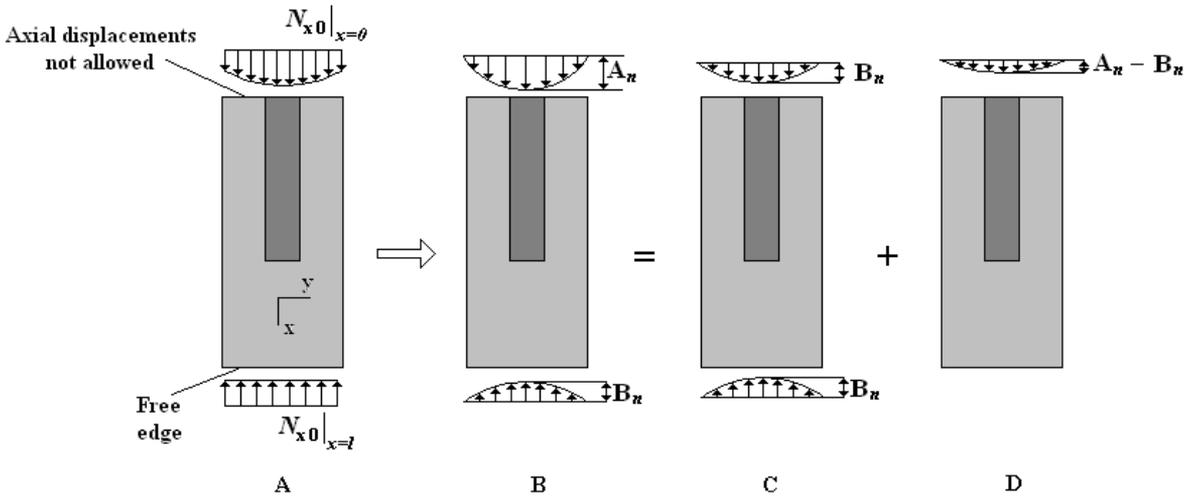
Figure 2. Loads on reinforced panel. (A) Constant axial load at the free edge. (B) Generalized Fourier series components of loads. (C) Uniform loading. (D) Reinforcement perturbation. The first component is shown for illustrative purposes only.

where I is the identity matrix. There are $N \times M$ eigenvalues λ_i and associated eigenvectors $W_{\text{cr},i}$. The lowest eigenvalue $\lambda_{\text{cr,min}}$ and its associated eigenvector $W_{\text{cr,min}}$ are related to the buckling loads N_{cr} and to the buckling mode shape w_{cr} by

$$N_{\text{cr}} = \lambda_{\min} \begin{bmatrix} N_{x0} \\ N_{y0} \\ N_{xy0} \end{bmatrix}, \qquad w_{\text{cr}} = \sum_{j=1}^{M_w \times N_w} \varphi_j (W_{\text{cr,min}})_j. \tag{25}$$

To solve the eigenvalues problem of (24), one must be able to integrate the expressions in (16), (22), and (23). This can only be done if the internal in-plane loads distribution in known throughout the domain. This load distribution is evaluated in the following section.

3. In-plane stress function

Consider the simple case, illustrated in Figure 2, of a composite assembly made of a skin (light gray area) and a reinforcement patch (dark gray area).

The panel is loaded by a constant axial load $N_{x0,l}$ acting upon the free edge ($x = l_x$). If an axial constraint acts on the opposite edge ($x = 0$), the axial load distribution (reaction) is not known a priori on that edge. The curve depicted in Figure 2A shows a potential $N_{x0,0}$ distribution on the edge $x = 0$. A peak in the region of the reinforced area is expected.

The magnitude of the peak load mostly depends on the axial stiffness ratio between the skin and the patch, and on the dimensions of the patch. Typically, if the patch free tip is sufficiently far from the constraint, we can assume that the local axial load transfer from the skin to the skin-patch region is complete; therefore the load is introduced in the skin-patch section proportionally to the local-to-global axial stiffness ratio. Assuming that the axial flow distribution N_{x0} at the constrained edge is known, let

us decompose the external edge loads by means of Fourier series:

$$N_{xo}\big|_{x=0} \cong \sum_{n=1}^{\overline{N}} A_n \sin(\alpha_n y), \qquad N_{xo}\big|_{x=l_x} \cong \sum_{n=1}^{\overline{N}} B_n \sin(\alpha_n y). \tag{26}$$

The two series expansions are generally different if compared term by term (Figure 2B), but since the global equilibrium is satisfied

$$\sum_{n=1}^{\overline{N}} \int_0^{l_y} A_n \sin(\alpha_n y) = \sum_{n=1}^{\overline{N}} \int_0^{l_y} B_n \sin(\alpha_n y). \tag{27}$$

Using the principle of superposition, two stress fields are combined. These are:

(1) a constant axial stress field equal to the constant axial load $N_{x0,0}$ acting upon the free edge $x = l_x$ (Figure 2C).

(2) a perturbation $\Delta N_x = N_{x0,l} - N_{x0,0}$ caused by the presence of the reinforcement (Figure 2C) and acting as an external load on the constrained edge.

The first stress field is constant and represents a panel made of a skin only; therefore it is equilibrated and compatible. The elastic problem is completely determined by introducing the stress function Ψ

$$\Psi = \Gamma_x N_{x0,l} + \Gamma_{xy} N_{xy0} + \Gamma_y N_{y0}, \tag{28}$$

where Γ_x, Γ_{xy}, and Γ_y are the circulation functions [Jaunky et al. 1995] defined as

$$\Gamma_x = (y - l_y)^2, \qquad \Gamma_{xy} = -(x - l_x)(y - l_y), \qquad \Gamma_y = (x - l_x)^2. \tag{29}$$

The second stress field represents a perturbation introduced by the presence of the reinforcement. It is equilibrated, according to (27), but, in general, is not compatible.

Introducing a perturbation stress function $\Delta\Psi$

$$\Delta N_x = \Delta\Psi_{,yy}, \qquad \Delta N_y = \Delta\Psi_{,xx}, \qquad \Delta N_{xy} = -\Delta\Psi_{,xy} \tag{30}$$

then if no body forces are acting, then overall equilibrium is represented by the biharmonic equation

$$\frac{\partial^4 \Delta\Psi}{\partial y^4} + 2\frac{\partial^4 \Delta\Psi}{\partial x^2 \partial y^2} + \frac{\partial^4 \Delta\Psi}{\partial x^4} = 0 \tag{31}$$

which is satisfied by

$$\Delta\Psi_n = \sin\left(n\pi \frac{y}{l_y}\right) f_n(x). \tag{32}$$

Substituting (31) into (30) and defining $\alpha_n = n\pi y / l_y$ creates the following ordinary differential equation:

$$\alpha_n^4 f_n(x) - 2\alpha_n^2 f_n^{II}(x) + f_n^{IV}(x) = 0 \tag{33}$$

with the solution

$$f_n(x) = c_{1n} \cosh(\alpha_n x) + c_{2n} \sinh(\alpha_n x) + c_{3n} x \cosh(\alpha_n x) + c_{4n} x \sinh(\alpha_n x). \tag{34}$$

Hence, the stress function is

$$\Delta\Psi_n = \left(c_{1n}\cosh(\alpha_n x) + c_{2n}\sinh(\alpha_n x) + c_{3n}x\cosh(\alpha_n x) + c_{4n}x\sinh(\alpha_n x)\right)\sin(\alpha_n x). \quad (35)$$

Constants c_{in} are calculated by enforcing the boundary conditions. First, the distribution of ΔN_{x0} along the edge $x = 0$ must be determined. Rationales for calculation of piece-wise distribution of N_{x0} are given in Appendix B. Knowing the axial flow piecewise distribution at the constrained edge (Figure 2A), and making use of a Galerkin technique [Cosentino and Weaver 2008], the external axial load distributions can be expressed as a generalized Fourier series

$$\Delta N_{xo}\Big|_{x=0_x} \cong \sum_{n=1}^{\bar{N}} (A_n - B_n)\sin(\alpha_n y), \qquad \Delta N_{xo}\Big|_{x=l_x} \cong 0. \quad (36)$$

Using the principle of superposition, we assume that the solution, in terms of stress functions, is given by the superposition of $\bar{N}$ basic stress functions $\Delta\Psi_n$ that are solutions of the elastic problem illustrated in Figure 2D.

$$\Delta\Psi = \sum_{n=1}^{\bar{N}} \Delta\Psi_n, \quad (37)$$

where the $\Delta\Psi_n$ are given by (32) and the load amplitudes are given by (36). Following [Timoshenko and Goodier 1982], the constants of integration in (35) are determined by enforcing the following boundary conditions:

For $x = 0$:

$$\Delta N_{xy,n} = -\frac{\partial^2\Delta\Psi_n}{\partial x\,\partial y} = 0, \qquad \Delta N_{x,n} = \frac{\partial^2\Delta\Psi_n}{\partial y^2} = A_n - B_n. \quad (38)$$

For $x = l_x$:

$$\Delta N_{xy,n} = -\frac{\partial^2\Delta\Psi_n}{\partial x\,\partial y} = 0, \qquad \Delta N_{x,n} = \frac{\partial^2\Delta\Psi_n}{\partial y^2} = 0. \quad (39)$$

After algebraic manipulations, coefficients of integration are obtained and expressed as

$$c_{1n} = \lambda_{1n}(A_n - B_n), \quad c_{2n} = \lambda_{2n}(A_n - B_n), \quad c_{3n} = \lambda_{3n}(A_n - B_n), \quad c_{4n} = \lambda_{4n}(A_n - B_n),$$

where

$$\lambda_{1n} = \frac{1}{\alpha_n^2}, \quad \lambda_{2n} = \frac{1 - \omega_{1n}\sinh(\alpha_n l_x)}{l_x\alpha_n^3}, \quad \lambda_{3n} = \frac{1 - (\omega_{1n}/\omega_{21n})\sinh(\alpha_n l_x)}{l_x\alpha_n^2}, \quad \lambda_{4n} = -\frac{\sinh(\alpha_n l_x)}{l_x\alpha_n\omega_{2n}} \quad (40)$$

and

$$\omega_{1n} = \frac{\cot\alpha_n}{\alpha_n} + \frac{1}{l_x\alpha_n^2}, \qquad \omega_{2n} = \left(\sin\alpha_n - l_x\alpha_n\cos\alpha_n\right)\omega_{1n} + l_x\sin\alpha_n. \quad (41)$$

It must be emphasized that solutions $\Delta\Psi_n$ do not identically satisfy term-by-term x-wise equilibrium of the panels as, in general, $A_n \neq B_n$, but their summation does satisfy overall equilibrium. In fact,

$$\sum_{n=1}^{\bar{N}} (A_n - B_n)\sin(\alpha_n y) \cong 0. \quad (42)$$

Also, these stress functions satisfy the natural boundary conditions, given in Figure 2A, that is, only axial loads are acting. At the edges $y = 0$ and $y = l_y$, N_{y0} are zero and only shear forces N_{xy} are present, arising from each term in (37), necessary to satisfy x-wise equilibrium. Note that (42) implies that summation of shears due to its n components is zero [Timoshenko and Goodier 1982, pp. 53–56].

To account for the presence of external shears N_{xy0} and y-wise loads N_{y0}, which were neglected so far, the stress function Ψ defined in (28) must be added. To this end, the resultant stress function Ψ_e is

$$\Psi_e = \Psi + \sum_{n=1}^{\bar{N}} \Delta \Psi_n. \tag{43}$$

This function satisfies the biharmonic equilibrium equation

$$\frac{\partial^4 \Psi_e}{\partial y^4} + 2\frac{\partial^4 \Psi_e}{\partial x^2 \partial y^2} + \frac{\partial^4 \Psi_e}{\partial x^4} = 0. \tag{44}$$

The resultant stress function Ψ_e is determined once coefficients A_n and B_n are derived. It satisfies the equilibrium equation (44) and the boundary conditions (38)–(39), but it does not satisfy the compatibility condition. To enforce compatibility, a supplementary stress function Ψ_c is superposed. This additional stress function must satisfy the boundary conditions (38)–(39) and guarantee that the resultant stress function Ω

$$\Omega = \Psi_e + \Psi_c \tag{45}$$

satisfies the compatibility equation.

The equilibrium and boundary conditions are fulfilled by choosing the supplementary stress function as

$$\Psi_c = \sum_{k=1}^{M_c \times N_c} \eta_k(x, y)\xi_k, \tag{46}$$

where ξ_k are unknown coefficients and $\eta_k(x, y)$ are defined as

$$\eta = \begin{bmatrix} X_{c,1}Y_{c,1} & X_{c,1}Y_{c,2} & \cdots & X_{c,1}Y_{c,N_{ce_w}} \\ & & & \\ X_{c,2}Y_{c,1} & X_{c,2}Y_{c,2} & \cdots & X_{c,2}Y_{c,N_{c_w}} & \cdots & X_{c,M_{c_w}}Y_{c,1} & \cdots & X_{c,M_c}Y_{c,N_c} \end{bmatrix}^T. \tag{47}$$

If abrupt variations of cross section occur within the domain, the linearized compatibility condition is expressed by [Ashton et al. 1969]

$$\frac{\partial^2}{\partial y^2}(A_{11}^*\Omega_{,yy} + A_{12}^*\Omega_{,xx} - A_{16}^*\Omega_{,xy}) + \frac{\partial^2}{\partial x^2}(A_{12}^*\Omega_{,yy} + A_{22}^*\Omega_{,xx} - A_{26}^*\Omega_{,xy})$$
$$+ \frac{\partial^2}{\partial x \, \partial y}(-A_{16}^*\Omega_{,yy} - A_{26}^*\Omega_{,xx} + A_{66}^*\Omega_{,xy}) = 0. \tag{48}$$

Differentiation and reordering gives

$$A_{11}^*\Omega_{,yyyy} - 2A_{26}^*\Omega_{,xyyy} + (2A_{12}^* + A_{66}^*)\Omega_{,xxyy} - 2A_{26}^*\Omega_{,xxxy} + A_{22}^*\Omega_{,xxxx} + (2A_{11,y}^* - A_{16,x}^*)\Omega_{,yyy}$$
$$+ (2A_{12,x}^* - 3A_{16,y}^* + A_{66,x}^*)\Omega_{,xyy} + (2A_{12,y}^* - 3A_{26,x}^* + A_{66,y}^*)\Omega_{,xxy} + (2A_{22,x}^* - A_{26,y}^*)\Omega_{,xxx}$$
$$+ (A_{11,yy}^* + A_{12,xx}^* - A_{16,xy}^*)\Omega_{,yy} - (A_{16,yy}^* + A_{26,xx}^* - A_{66,xy}^*)\Omega_{,xy} + (A_{12,yy}^* + A_{22,xx}^* - A_{26,xy}^*)\Omega_{,xx}$$
$$= 0. \tag{49}$$

The coefficients ξ_k are determined by solving (46) by means of a Galerkin technique [Cosentino and Weaver 2008]. The weight functions employed are

$$\phi_n(x, y) = \Psi_e(x, y) + \eta_n(x, y). \tag{50}$$

Substituting (45) into (49) and carrying out the differentiations, then after algebraic manipulations we obtain the compact form

$$\mathbf{\Xi}\boldsymbol{\xi} = \boldsymbol{L}, \tag{51}$$

where

$$\boldsymbol{\xi} = [\xi_1\xi_2, \ldots, \xi_{N_c \times M_c}]^T, \tag{52}$$

$$
\begin{aligned}
(\mathbf{\Xi})_{ij} = \int_0^{l_x} \int_0^{l_y} \Bigg(& A_{11}^* \frac{\partial^4 \Psi_{c,j}}{\partial y^4} - 2A_{26}^* \frac{\partial^4 \Psi_{c,j}}{\partial x\,\partial y^3} + (2A_{12}^* + A_{66}^*)\frac{\partial^4 \Psi_{c,j}}{\partial x^2\partial y^2} - 2A_{26}^* \frac{\partial^4 \Psi_{c,j}}{\partial x^3\partial y} \\
& + A_{22}^* \frac{\partial^4 \Psi_{c,j}}{\partial x^4} + (2A_{11,y}^* - A_{16,x}^*)\frac{\partial^3 \Psi_{c,j}}{\partial y^3} + (2A_{12,x}^* - 3A_{16,y}^* + A_{66,x}^*)\frac{\partial^3 \Psi_{c,j}}{\partial x\,\partial y^2} \\
& + (2A_{12,y}^* - 3A_{26,x}^* + A_{66,y}^*)\frac{\partial^3 \Psi_{c,j}}{\partial x^2\partial y} + (2A_{22,x}^* - A_{26,y}^*)\frac{\partial^3 \Psi_{c,j}}{\partial x^3} \\
& + (A_{11,yy}^* + A_{12,xx}^* - A_{16,xy}^*)\frac{\partial^2 \Psi_{c,j}}{\partial y^2} - (A_{16,yy}^* + A_{26,xx}^* - A_{66,xy}^*)\frac{\partial^2 \Psi_{c,j}}{\partial x\,\partial y} \\
& + (A_{12,yy}^* + A_{22,xx}^* - A_{26,xy}^*)\frac{\partial^2 \Psi_{c,j}}{\partial x^2} \Bigg)\phi_i\,dy\,dx,
\end{aligned}
\tag{53}
$$

and

$$
\begin{aligned}
\boldsymbol{L}_i = -\int_0^{l_x} \int_0^{l_y} \Bigg(& A_{11}^* \frac{\partial^4 \Psi_e}{\partial y^4} - 2A_{16}^* \frac{\partial^4 \Psi_e}{\partial x\,\partial y^3} + (2A_{12}^* + A_{66}^*)\frac{\partial^4 \Psi_e}{\partial x^2\partial y^2} - 2A_{26}^* \frac{\partial^4 \Psi_e}{\partial x^3\partial y} \\
& + A_{22}^* \frac{\partial^4 \Psi_e}{\partial x^4} + (2A_{11,y}^* - A_{16,x}^*)\frac{\partial^3 \Psi_e}{\partial y^3} + (2A_{12,x}^* - 3A_{16,y}^* + A_{66,x}^*)\frac{\partial^3 \Psi_e}{\partial x\,\partial y^2} \\
& + (2A_{12,y}^* - 3A_{26,x}^* + A_{66,y}^*)\frac{\partial^3 \Psi_e}{\partial x^2\partial y} + (2A_{22,x}^* - A_{26,y}^*)\frac{\partial^3 \Psi_e}{\partial x^3} \\
& + (A_{11,yy}^* + A_{12,xx}^* - A_{16,xy}^*)\frac{\partial^2 \Psi_e}{\partial y^2} - (A_{16,yy}^* + A_{26,xx}^* - A_{66,xy}^*)\frac{\partial^2 \Psi_e}{\partial x\,\partial y} \\
& + (A_{12,yy}^* + A_{22,xx}^* - A_{26,xy}^*)\frac{\partial^2 \Psi_e}{\partial x^2} - (A_{16,yy}^* + A_{26,xx}^* - A_{66,xy}^*)\frac{\partial^2 \Psi_e}{\partial x\,\partial y} \\
& + (A_{12,yy}^* + A_{22,xx}^* - A_{26,xy}^*)\frac{\partial^2 \Psi_e}{\partial y^2} \Bigg)\phi_i\,dx\,dy.
\end{aligned}
\tag{54}
$$

The components of vector $\boldsymbol{L}$ are computed once the equilibrium stress function (43) is derived. They are functions of the external loads $N_{x,0}$, $N_{y,0}$, and $N_{xy,0}$, and act as load terms in (49).

To calculate partial derivatives of the components A_{ij}^* of the in-plane compliance matrix, a Galerkin technique [Cosentino and Weaver 2008] is employed to express such components as generalized Fourier

series

$$A_{ij}^* = \sum_{k=1}^{M \times N} \omega_{ij,k} \bar{\varphi}_k, \tag{55}$$

where the same basis functions $\bar{\varphi}_k$ already used for the eccentricity are employed.

4. Model validation: in-plane stress field

A composite assembled panel (Figure 3) consisting of a square skin and a rectangular reinforcement (patch) was analyzed to compare and validate our analysis against finite element models (FEM). The in-plane stress field calculated by means of the proposed analytical solution was first compared with the finite element response. In-plane normal forces arising along the sections indicated in Figure 3, right, were compared for two different load cases. The finite element simulation was done using ABAQUS. The domain was discretized using quadratic quadrilateral elements (S8R) in a regular array. Each square has a 2.5 mm edge length. An offset was assigned to all the elements that represent the skin-reinforcement overlap region. The offset equals the difference of the two x-wise neutral planes, overlap and skin regions, respectively. The material properties of the lamina (patch and skin) are given by

$$E_L = 150000 \, \text{MPa}, \quad E_T = 8800 \, \text{MPa}, \quad G_{LT} = 4800 \, \text{MPa}, \quad \nu_{LT} = 0.35 \, , \quad \text{thickness} = 0.2 \, \text{mm}.$$

The geometrical parameters are

$$l_x = 100 \, \text{mm}, \quad l_y = 100 \, \text{mm}, \quad l_P = 40 \, \text{mm}, \quad b = 20 \, \text{mm}.$$

The stacking sequences are

$$\text{patch: } [0/90/45/-45]_S, \quad \text{skin: } [0/90]_S$$

The enforced boundary conditions are summarized in Table 1. The following sets of functions were employed to model the compatibility stress function Ψ_c and the eccentricity e^2:

$$X_{c,i} = \sin \frac{i \pi x}{l_x}, \quad Y_{c,j} = \sin \frac{j \pi y}{l_y}, \quad \bar{X}_i = 1 - \cos \frac{i \pi (l_x - x)}{2 l_x}, \quad \bar{Y}_j = \sin \frac{j \pi y}{l_y}. \tag{56}$$

The same set of eigenfunctions is used to model both the eccentricity and the components of the in-plane flexibility A_{ij}^*. A total of 10 eigenfunctions for each coordinate were employed to expand the supplementary stress function and A_{ij}^*. Similarly, 10 functions were used to calculate and express the equilibrium stress function Ψ_e.
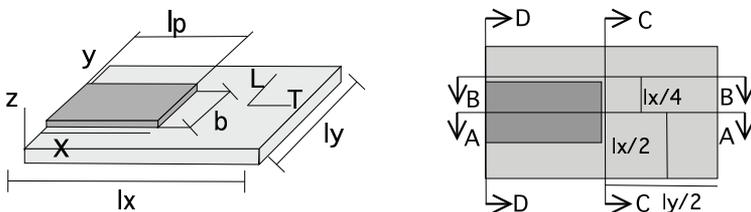
Figure 3. Reinforced panel: geometry (left) and plant view (right).

	Edge	Degrees of freedom				
		u_x	u_y	φ_x	φ_y	w
Load case A	a	restrained	restrained	free	—	restrained
	b	free	free	—	free	restrained
	c	free	restrained	free	—	restrained
	d	free	free	—	free	restrained
Load case B	a	restrained	restrained	free	—	restrained
	b	free	restrained	—	free	restrained
	c	free	restrained	free	—	restrained
	d	free	restrained	—	free	restrained

Table 1. Boundary conditions for in-plane stress field experiments.

The first comparison was carried out by imposing a negative unitary axial displacement to the edge c (Figure 4, left). Edges b and d are free to displace in the y-direction. Analytical and FEM results are reported in Figure 5, top. Boundary conditions are indicated in Table 1. For the second load case, a negative unit axial displacement was again enforced to edge b, but this time the y-wise displacements were restrained along the edges b and d. Results are reported in Figure 5, bottom.

Correlation between FEM and the proposed analytical model is generally very good for both cases. The overlap region is characterized by a considerable amount of in-plane axial load N_x, significantly larger than the far field applied load. Conversely, a noteworthy decrease of the axial load is observed in the portions of the skin that are adjacent to the reinforcement. This result is approximately predicted by assuming that the axial strains and displacements do not vary y-wise Appendix A, and it is confirmed by finite element results.

We stress that the predicted axial load transfer at the reinforcement tip is slightly smoother than the transfer calculated by finite element analysis. This is mostly caused by the generalized Fourier series expansion used to model both the compatibility stress function Ψ_c and the components of the in-plane flexibility A_{ij}^* and their partial derivatives.
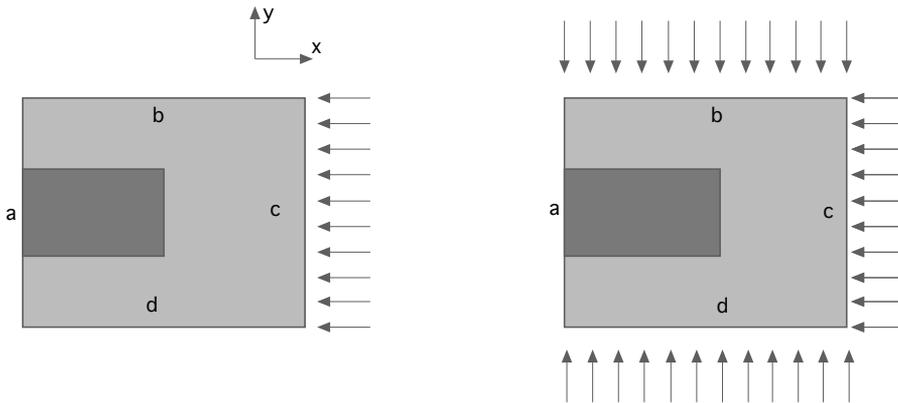
Figure 4. Load cases for in-plane stress field experiments: pure compression (left) and biaxial compression (right).
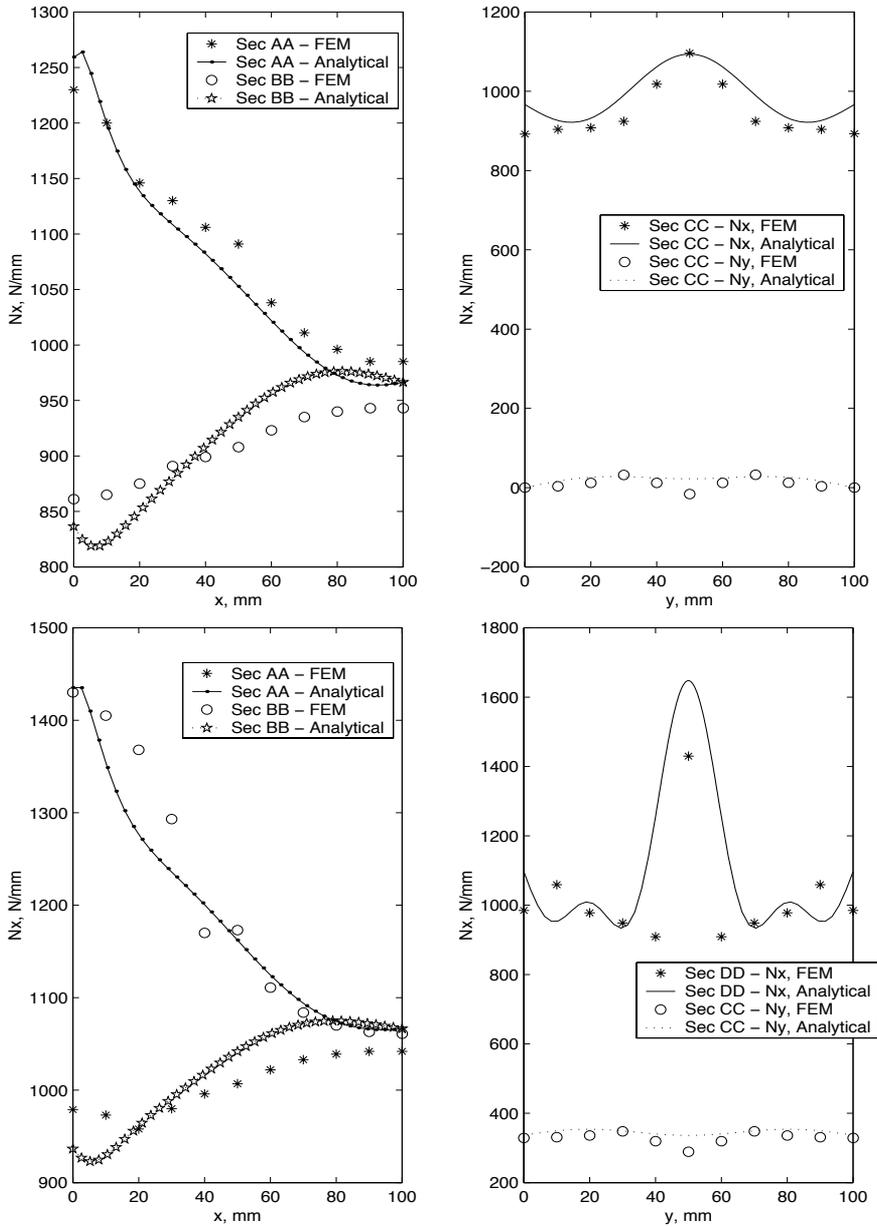
Figure 5. In-plane stress resultant correlation. Top, load case A; bottom, load case B. Left: sections AA and BB; right, section CC.

5. Model validation: convergence study and buckling loads

In order to validate the analytical calculation of critical buckling loads, a series of comparisons with finite element analysis were carried out for five different load cases. The reference structure is the same composite assembly previously analyzed in Section 4. The load cases studied are shown in Figure 6, and
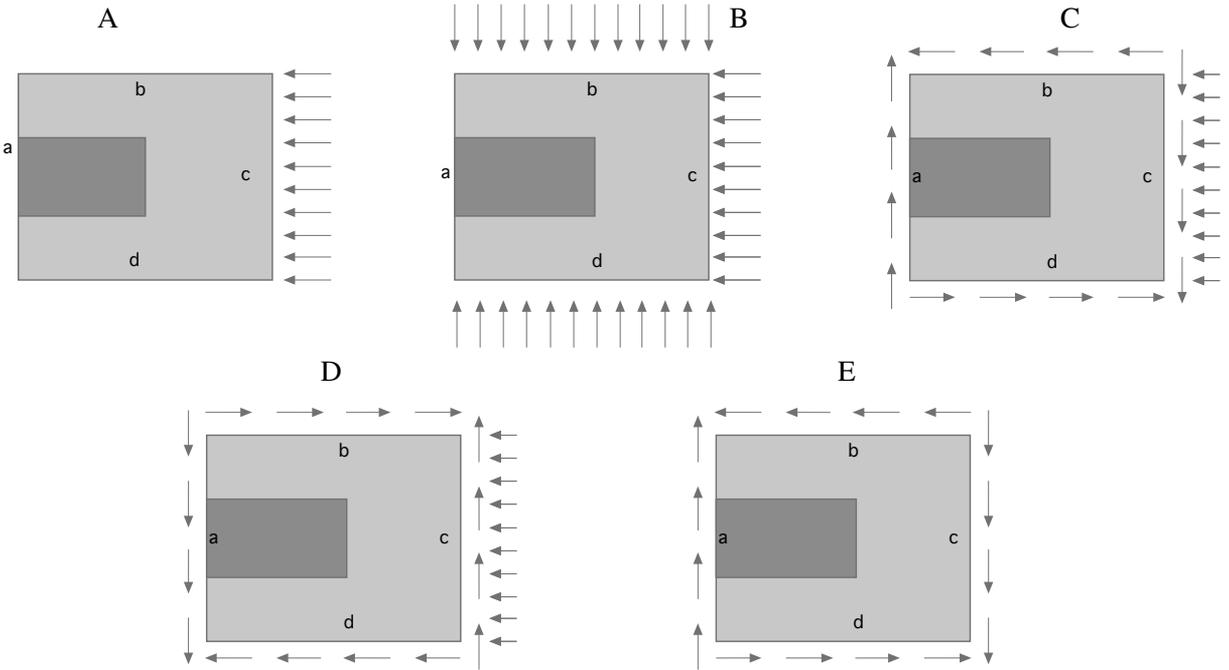
Figure 6. Load cases for buckling load study. Top: pure compression (left); biaxial compression (middle); combined shear-compression (right). Bottom: combined shear-compression with reverted shear (left); pure shear (right).

can be described as follows:

A. axial compression;

B. biaxial compression;

C. combined shear and axial compression, shear/compression ratio equal to 1 ;

D. combined shear and axial compression, shear/compression ratio equal to -1;

E. pure shear.

For each load case analyzed, corresponding boundary conditions are reported in Table 2. The eigenfunctions used to model the compatibility stress function Ψ_c are

$$X_{c,i} = \sin \frac{i\pi x}{l_x}, \qquad Y_{c,j} = \sin \frac{j\pi y}{l_y}. \tag{57}$$

Since the in-plane stress field cannot be assumed to be uniaxial, the same number of eigenfunctions was used for both the x- and y-directions ($M = N$).

Furthermore, to quantify the degree of accuracy provided by making use of the supplementary stress function, two different buckling analyses were carried out and compared with finite element results. The relative efficiencies of both solution techniques: the equilibrium solution (43) or the equilibrated and compatible solution (45) were assessed. Two different analytical solutions were calculated and compared

	Edge	Degrees of freedom				
		u_x	u_y	φ_x	φ_y	w
Load case A	a	restrained	restrained	free	—	restrained
	b	free	free	—	free	restrained
	c	free	restrained	free	—	restrained
	d	free	free	—	free	restrained
Load case B	a	restrained	restrained	free	—	restrained
	b	free	restrained	—	free	restrained
	c	free	restrained	free	—	restrained
	d	free	restrained	—	free	restrained
Load case C	a	restrained	restrained	free	—	restrained
	b	free	free	—	free	restrained
	c	free	free	free	—	restrained
	d	free	free	—	free	restrained
Load case D	a	restrained	restrained	free	—	restrained
	b	free	free	—	free	restrained
	c	free	free	free	—	restrained
	d	free	free	—	free	restrained
Load case E	a	restrained	restrained	free	—	restrained
	b	free	free	—	free	restrained
	c	free	free	free	—	restrained
	d	free	free	—	free	restrained

Table 2. Boundary conditions for buckling load experiments.

with finite element response. It is noted that the use of solution (43) does not require the compatibility equation (49) to be solved. Hence, it is significantly more efficient in terms of calculation time. Yet, the resultant stress function (45) is expected to be appreciably more accurate.

The first buckling analysis is done by solving (24) and calculating the critical minimum eigenvalues. Expressions for in-plane stress resultants are given by

$$N_x = \Omega_{,yy}, \qquad N_y = \Omega_{,xx}, \qquad N_{xy} = -\Omega_{,xy}. \tag{58}$$

The second analytical calculation was carried out by neglecting the compatibility equation and arresting the in-plane stress field calculation to the determination of the equilibrium stress function only. In this latter case, the in-plane stress resultants are

$$N_x = \Psi_{e,yy}, \qquad N_y = \Psi_{e,xx}, \qquad N_{xy} = -\Psi_{e,xy}. \tag{59}$$

Both the equilibrated and the equilibrated and compatible solutions were compared with finite element responses. The finite element model is the same as that employed in the previous section. The critical minimum eigenvalues found analytically were divided by the critical eigenvalues calculated by means of
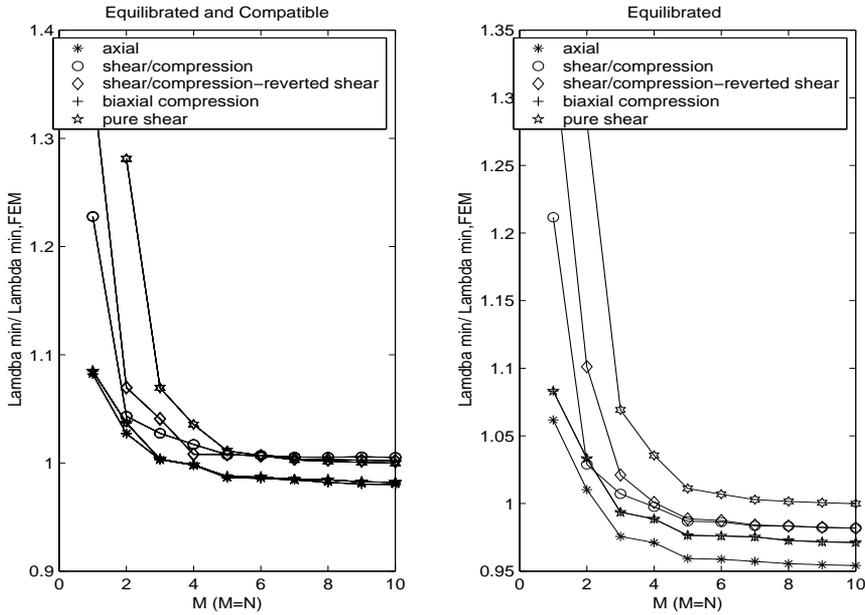
Figure 7. Convergence study: equilibrated and compatible solution (left); equilibrated solution (right).

FEM and results are reported in Figure 7. The sensitivity of both solutions to the total number of functions used to expand the transverse displacement and the compatibility stress function was studied to verify the convergence rate. Both solutions converge with five or more eigenfunctions, but the convergence rate and the accuracy obtained by employing the combined equilibrated and compatible solution are improved. However, the degree of accuracy is more than acceptable for both cases.

A further comparison between the two solutions is presented. The error discrepancy is plotted against the total time required to complete the analysis and results are reported in Figure 8. The error is defined as

$$\text{error} = \frac{\lambda_{\min} - \lambda_{\min,\text{FEM}}}{\lambda_{\min,\text{FEM}}} \times 100\%. \tag{60}$$

Despite guaranteeing better degree of accuracy and faster convergence rates, the use of the compatibility stress function implies calculation times that are between 80% and 90% greater than the calculation times required by solving the buckling problem making use of the equilibrium equation (27) only to determine the in-plane stress field. In the equilibrated and compatible case (Figure 8, left), the error induced is between −2.5% and 1.5% after 10 seconds of computation. In contrast, for the equilibrated case (Figure 8, right), the error is stably confined within a broader range (−4% to 2.5%), but after 4 seconds only. However, the computational effort required by either solution is negligible compared to those required by FEM, which were of more than 80 seconds per load case. (Naturally, the computation times reported do not include model set-up, which is also much larger in the case of FEM analysis.) The use of either solution techniques is shown to perform better than FEM. Of course, the degree of accuracy achievable is excellent if employed in a preliminary sizing phase of an aircraft design, when hundreds of load cases need to be analyzed. In such cases, a relatively simple parametric model may be
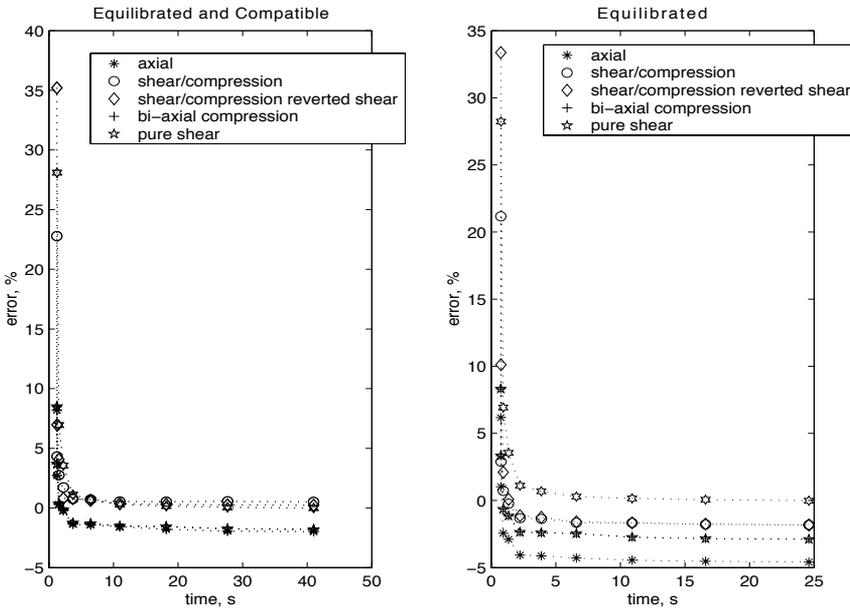
Figure 8. Calculation times: equilibrated and compatible solution (left); equilibrated solution (right).

more suitable than highly detailed analyses. It must be noted that, for each solution, at least half of the calculation time is utilized in computing the G matrix, as defined in (21). This matrix does not depend on the in-plane stress function, but only on the boundary condition assumed for the transverse displacement w. Therefore this calculation is only required once, and need not be repeated for different external loads.

6. Interaction curves and sensitivity analysis

To assess the sensitivity of buckling loads and mode shapes to the geometrical parameters and to the boundary conditions, additional analyses were carried out and compared with FEM. A typical aeronautical panel was taken as a baseline. A skin and a T-shaped stringer characterize the composite assembly. The stringer is run out as illustrated in Figure 9.
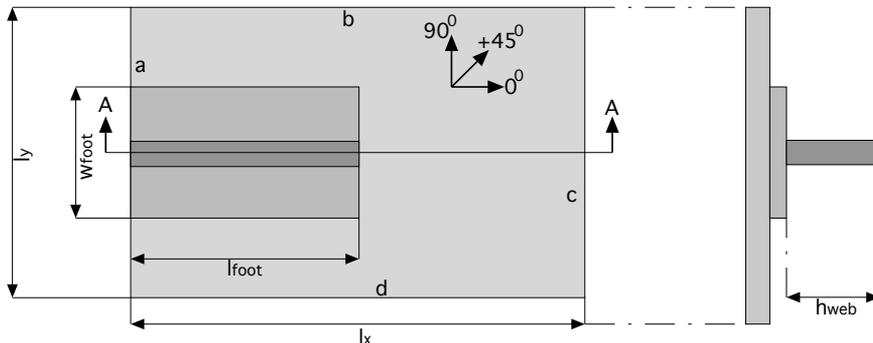
Figure 9. Panel geometry.

Geometry	Configuration	a	b	c	d
Baseline	B1	SS	SS	SS	SS
	B2	C	C	C	C
	B3	SS	C	SS	C
	B4	C	SS	C	SS

Table 3. Boundary conditions: SS = simply supported, C = clamped. (See Figure 9 for the edge labels a–d.)

The geometrical parameters of the baseline are

$$l_x = 300\,\text{mm}, \quad l_y = 200\,\text{mm}, \quad l_\text{foot} = 200\,\text{mm}, \quad w_\text{foot} = 40\,\text{mm}, \quad h_\text{web} = 20\,\text{mm}.$$

The stacking sequences are as follows (ply thickness = 0.2 mm in all cases):

skin: $[0/45/90/0/-45/0/90]_{2S}$;   foot: $[0/45/0/90/0/-45/0]_S$;   web: $[0/45/0/90/0/-45/0]_{2S}$.

For convenience, the same material properties as the ones were assumed as in Section 4; we list them again for convenience:

$$E_L = 150000\,\text{MPa}, \quad E_T = 8800\,\text{MPa}, \quad G_{LT} = 4800\,\text{MPa}, \quad \nu_{LT} = 0.35, \quad \text{thickness} = 0.2\,\text{mm}.$$

The first series of comparisons were carried out in order to assess the effect of several different boundary conditions. Several edge support configurations were studied, are listed in Table 3.

To assess the effect of flexural/twist anisotropy on buckling loads, the nondimensional parameters

$$\delta = \frac{D_{26}}{\sqrt[4]{D_{11}D_{22}^3}}, \qquad \gamma = \frac{D_{16}}{\sqrt[4]{D_{11}^3 D_{22}}}, \qquad \beta = \frac{D_{12} + 2D_{66}}{\sqrt{D_{11}D_{22}}} \tag{61}$$

(see [Weaver and Nemeth 2007]) were calculated for each subdomain, with results shown in Table 4. The values of δ and γ are much less than 0.1, indicating that flexural/twist anisotropy effects are small [Weaver and Nemeth 2007]. Furthermore, a value of $\beta < 1$ indicates relatively poor buckling performance compared with the quasiisotropic lay-up. As such, the lay-ups used are not highly efficient with respect to buckling resistance but do have relatively good axial strength characteristics (due to the relatively large percentage of 0° plies).

Subdomain	δ	γ	β
skin	0.03	0.0247	0.616
skin/foot	0.0153	0.0112	0.623
skin/foot/web	0.00063	0.00034	0.28
mean value	0.0283	0.0232	0.612

Table 4. Nondimensional parameters.

For each configuration, the smallest buckling loads were analytically calculated for a variety of shear/compression ratios and interaction curves were calculated and compared with finite element responses. Results are reported in Figure 10. Superposed are the values obtained from the interaction formula $R_x + R_s^{1.9+0.1\beta} \leq 1$, derived in [Weaver and Nemeth 2008] for long orthotropic plates under combined loading. Here x and s refer to the axial and shear load, respectively, and R represents the ratio of critical load for the combined-loading state to critical value of the corresponding load acting alone. Although this formula was not derived for buckling of panels with stringer run-outs under combined loading, the close match with the present analysis is notable.
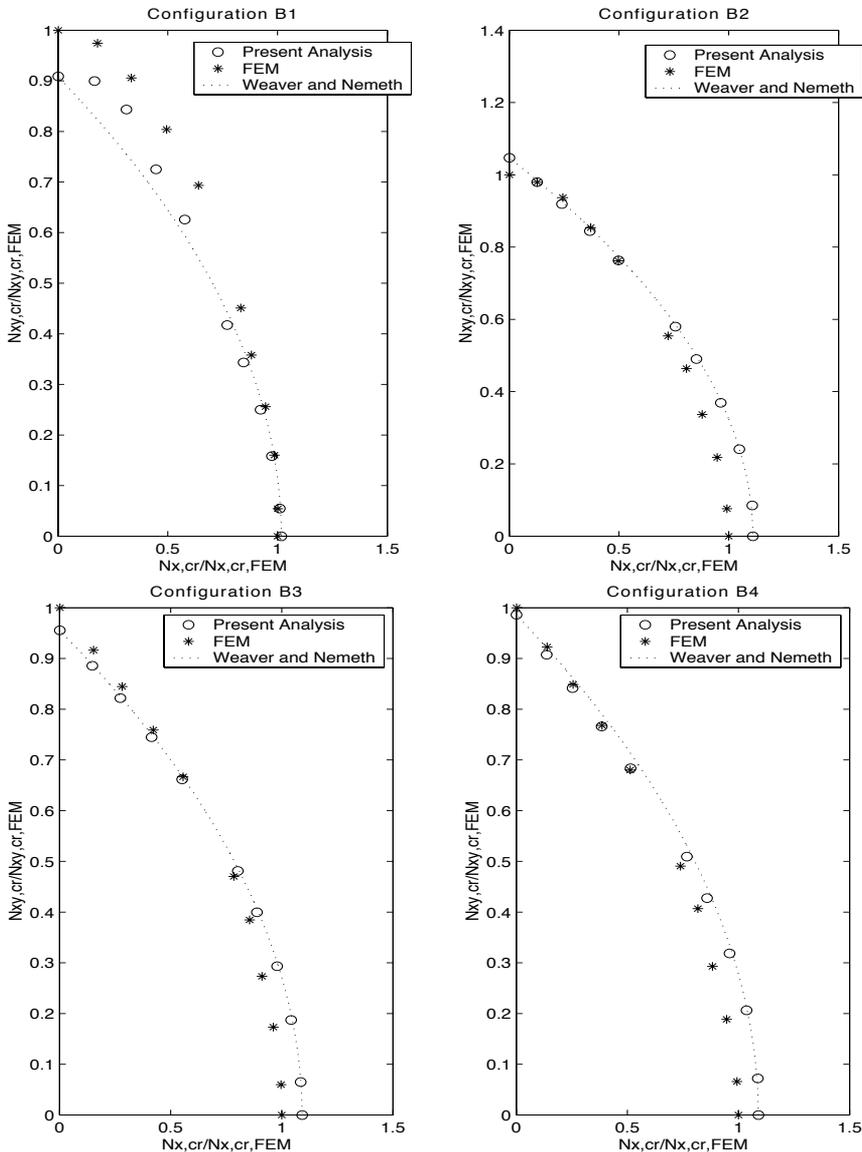
Figure 10. Interaction curves for configurations B1–B4 (top left to bottom right).

Comparisons show excellent correlation with FEM. However, a decrease of accuracy is noted with respect to the first simple configuration analyzed in Section 5. The analytical calculation shows an overall conservatism if compared with FEM, in the buckling loads prediction for configuration B1 (Figure 10, top left), where the induced error in the calculation of the buckling load under pure compression is negligible, while the shear buckling load is underestimated. In contrast, configurations B2 and B4 (right column in 10) show excellent correlation for the buckling loads under pure compression, but increasingly overpredict as the shear/compression ratio tends to zero. Finally, configuration B3 (Figure 10, bottom left) shows overestimated compression-buckling loads and slightly underestimated shear-buckling loads. However, it must be emphasized that the induced error is constant within the range -8% to $+10\%$ for all of the examined configurations and for all of the shear/compression rations. Calculation times were negligible and also possess the advantage provided by a fully parametric model. Finally, it is noted that the use of different sets of functions to model the out-of-plane displacement may reduce the induced error, but this analysis is beyond the scope of the present research.

Examples of analytically calculated mode shapes are provided in Figures 11 and 12 for there different loading and boundary conditions. Comparisons with FEM show that the shapes are adequately captured by the analytical model.

To assess the sensitivity of the panel's buckling loads to the geometrical parameters, additional sensitivity analyses were performed. In the first set of analyses, the effect of the panel length l_x was studied. Configurations B1 and B2 were analyzed and buckling loads were calculated under pure compression loading condition. Results are reported in Figure 13.

Comparisons show that the average trend is reasonably captured by the analytical approach. However, the effect of the panel x-wise length appears to be smoother in the analytical predictions than in FEM. For configuration B1, in the range of l_x between 300 mm and 250 mm, the buckling loads decrease as the total length decreases. The trend is then reversed in the lower range (l_x between 250 mm and 200 mm). With reference to Figure 9, mode shapes are plotted x-wise along the central Section AA. Results are reported in Figure 14. A noticeable change in the mode shapes occurs when the length varies from 300 mm to 260 mm (first three parts of Figure 14). While for long panels a buckling mode could occur which is localized in the skin in front of the run-out tip (Figure 14, top left), as the length decreases the buckling of the panel alters from a more localized mode involving part of the panel only (the skin
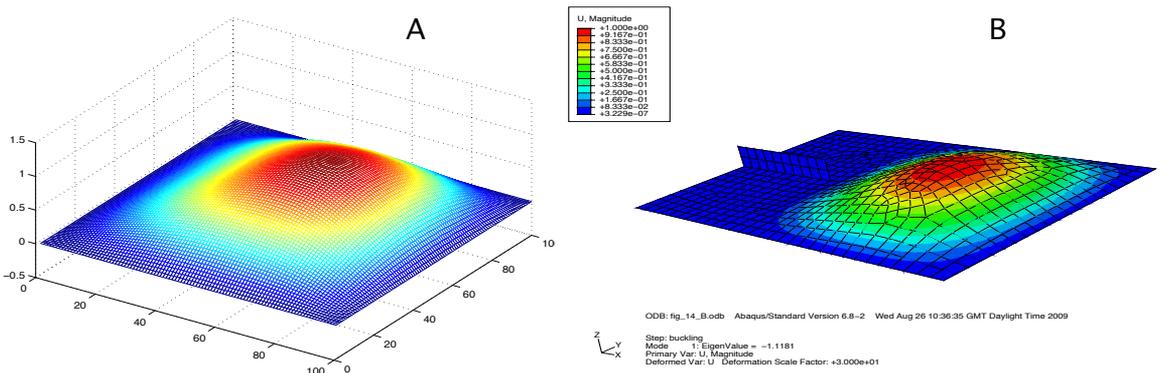
Figure 11. First buckling mode for configuration B1 under pure compression. Left: model; right: FEM.
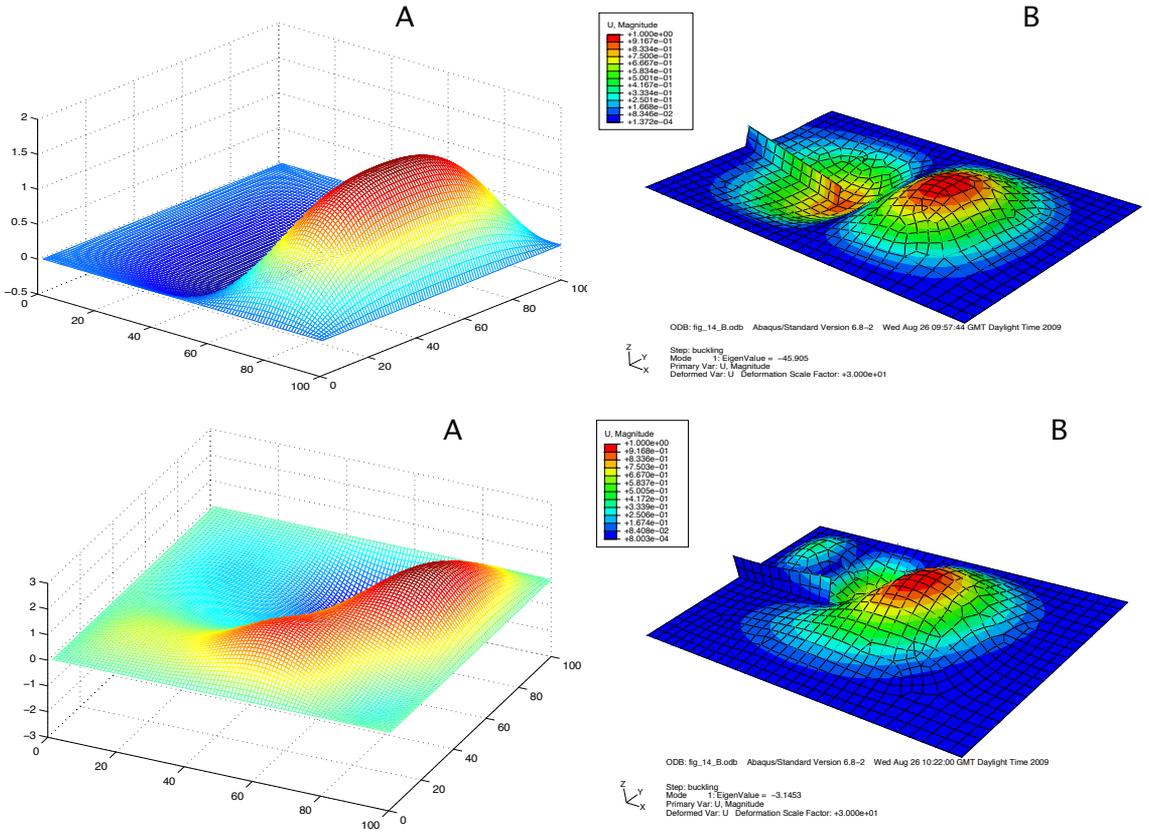
Figure 12. First buckling mode for configuration B2 under pure compression (top) and under combined shear and compression, ratio = 1 (bottom). Left: model; right: FEM.
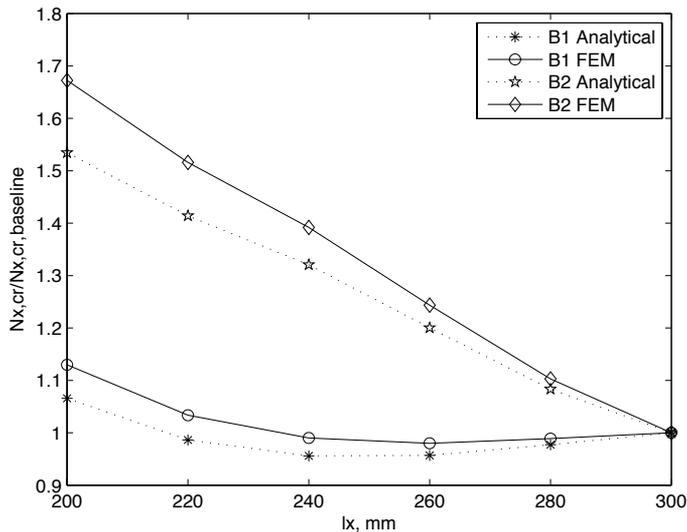
Figure 13. Buckling load sensitivity to panel length.

beyond the stiffener tip), to a more global phenomenon involving the stiffener. In this phase, the effective free x-wise length panel increases, hence a reduction of the buckling loads is observed. As the length continues to decrease, the buckling modes remain self-similar (that is, a global buckling mode with a single x-wise half wave) and the buckling loads increase (last three parts of Figure 14.) The buckling localisation for larger length is also believed to cause the interaction curve to significantly deviate from the formula proposed in [Weaver and Nemeth 2008], as seen in Figure 10, top left.
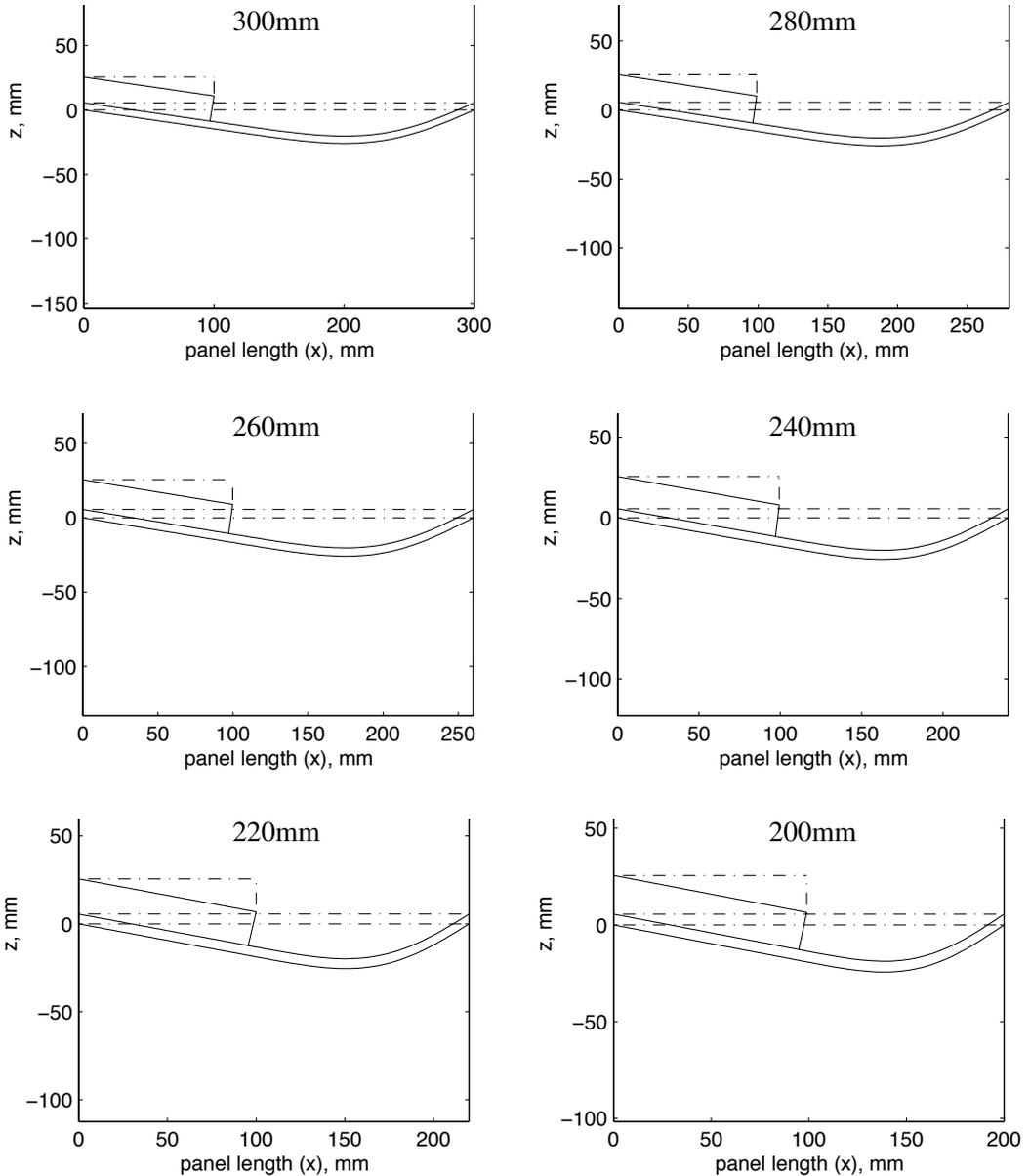
Figure 14. Mode I shapes (section AA) for panel B1 of x-wise lengths equal to 300, 280, 260, 240, 220 and 200 mm.

For configuration B2, the buckling loads increase almost linearly as the panel length decrease; the deformations are shown in Figure 15. When the length varies from an initial value of 300 mm to 260 mm, the buckling modes appear to be self-similar; therefore the buckling loads increase as the length decreases. As the length continues to decrease, a change in the mode shape occurs. Again, the buckling of the panel
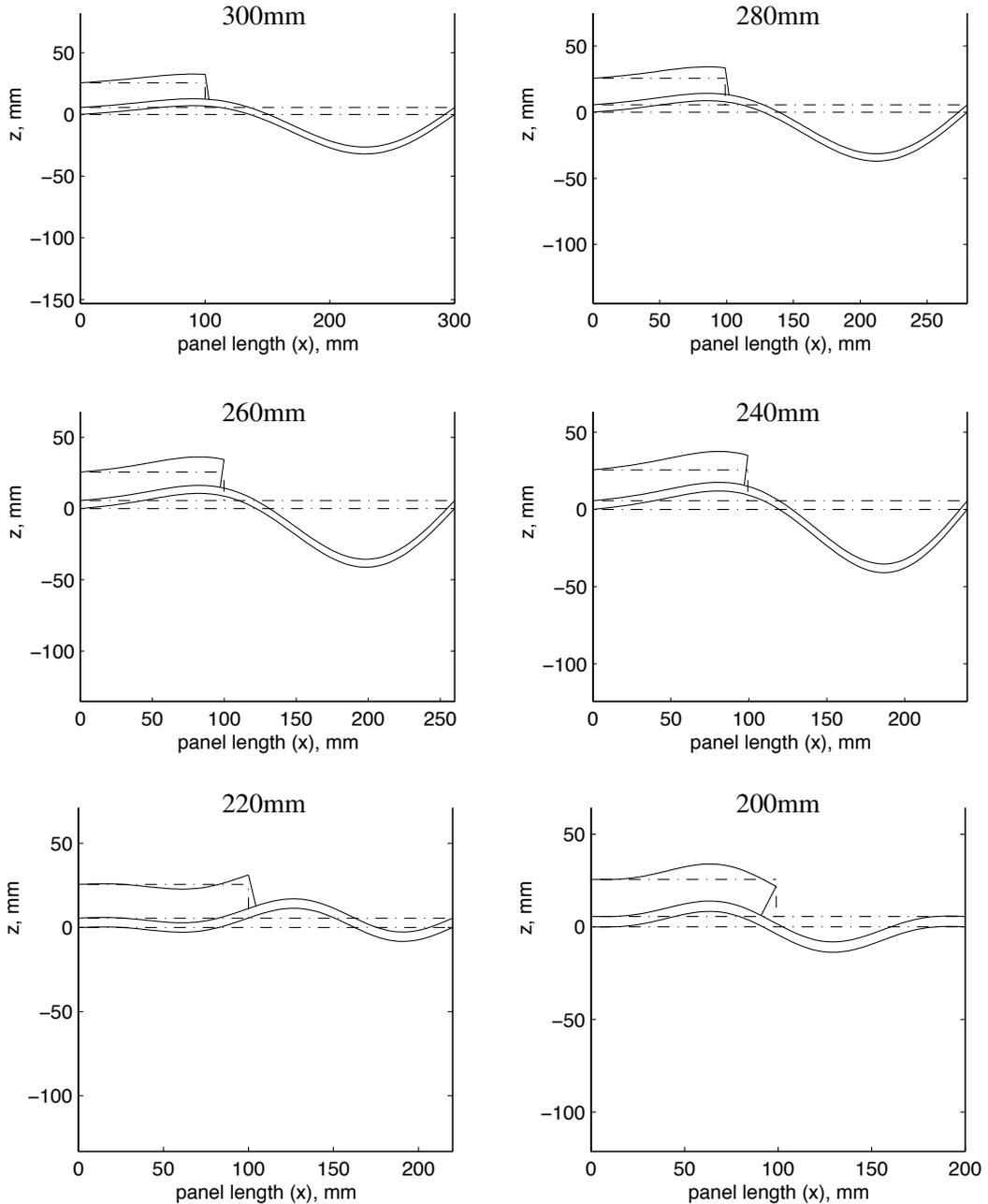
Figure 15. Mode I shapes (section AA) for panel B2 of x-wise lengths equal to 300, 280, 260, 240, 220 and 200 mm.
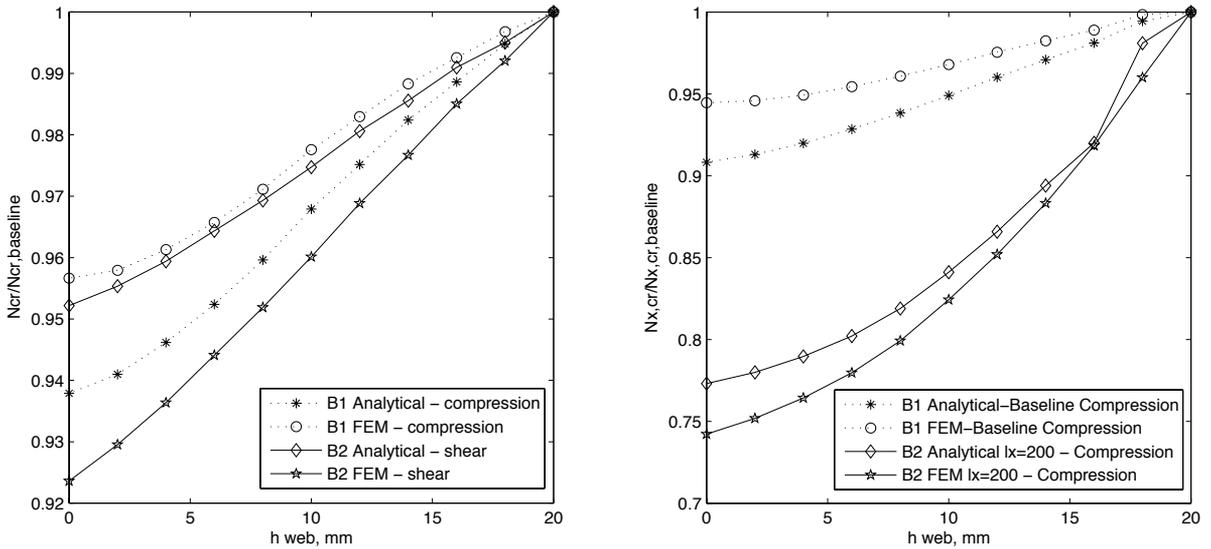
Figure 16. Buckling load sensitivity to web height.

alters from a two x-wise half waves phenomenon (more accentuated in the skin beyond the stiffener tip), to a more global phenomenon also involving the stiffener. The buckling loads then increase as the length decreases. The increase takes place at a smaller rate (Figure 13) as the amount of energy required to include the effects of the stiffener in the global deformation increases.

In the second set of analyses, the effect of the web height h_{web} was studied. Configurations B1 was analyzed in a first step and buckling loads were calculated under pure compression and pure shear loadings. Results are reported in Figure 16, left. A second set of analyses was carried out. The effect of h_{web} was assessed in configuration B2 under pure compression and with two different panel lengths: $l_x = 300$ mm (baseline geometry) and $l_x = 200$ mm. Results are reported in Figure 16, right. Comparison with FE analyses show that the trend is well captured by the analytical approach. It must be emphasized that, for configuration B2, short panels are significantly more sensitive to the web height than long panels (Figure 16, right). In fact, as already seen in Figure 15, the buckling modes of panels with lengths between 300 mm and 250 mm are characterized by two half waves with an accentuated transverse displacement that is localized in the free skin region in front of the stringer termination. For lengths that are below 250 mm, the panel buckles in to mode shapes, which are more global, that is, the web is characterized by increased transverse displacements. Therefore short panels are more sensitive to the web height than corresponding long configurations.

7. Discussion

The results presented in Section 6 generally show more than acceptable agreement between analysis and FEM. As shown in Figures 10–12, the present analysis guarantees good level of accuracy both in terms of buckling interaction curves and mode shape calculation. Although the method is in some cases slightly nonconservative (if compared to FEM) with regards to the calculation of buckling loads in pure compression, there is significant merit for the method in comparison with FEM.

(1) In preliminary phases of aircraft design, there is an objective need for simple analytical solutions that guarantee considerable reduction of computational effort. There are often many (often extending to hundreds) of load cases to consider as well as optimisation studies to be done. Currently, FEM is too computationally expensive to be employed for all load cases and optimisation studies, except for particular exemplar cases. The slight nonconservative nature of some of the results does not pose a significant problem for practical use by industry because predictions that are slightly non-conservative are factored by subsequent introduction of statistical and environmental knockdown factors.

(2) Despite the fact that FEM is able to provide realistic predictions, the large computational times associated in conjunction with the rather significant sensitivity of the results to the mesh size discourage its use as main tool for at least preliminary phases of aircraft design. In the present study no sensitivity analyses were undertaken to show that FEM predictions had converged and the mesh size was chosen based on the authors' engineering judgment (ref. to Figures 11 and 12). The employed mesh appears to be sufficiently refined to offer reasonably acceptable results within computational times, which are suitable for the purpose of this study. It is realistic to expect the use of more refined meshes for industrial purposes, which lead to much larger computational effort and time. The present analysis shows that computational times are already more than 10 times smaller than the ones associated with the use of coarse, two-dimensional FEM. This difference in analysis speed would be exacerbated if a more refined mesh were used, especially in conjunction with a fully three-dimensional model.

For the reasons described above, the present analysis is suitable for preliminary design calculations. To the best of our knowledge there are no analytical methods available in the literature, which predict the in-plane loads redistribution due to the presence of an incomplete stiffener terminated mid-bay along the bay length—a problem of significant interest to aircraft designers. It is recognized that further potential exploitations of the present analysis are also possible. For example, in cobonded and cocured composite assemblies, interlaminar shear stresses arising within the bond-line enable in-plane load transfer from the skin to the skin/stringer section. An extended model that also includes transverse shear stresses could be implemented and employed in conjunction with the present approach in order to provide fast and accurate calculation of interlaminar stresses.

8. Conclusions

A meshless approach was developed and used to predict local and global buckling of discretely assembled multibay composite panels made from skin and stiffeners. Numerical results obtained are compared with finite element analysis and show very good correlation in terms of in-plane loads distribution and buckling loads calculation. The use of either solution (equilibrated, and equilibrated and compatible) found for in-plane linear equilibrium appears to offer noteworthy level of accuracy and remarkable efficiency and flexibility compared with complementary finite element calculations. A robust and efficient method for quick evaluation of buckling loads of composite panels with stringer run-outs is presented. If used for industrial purposes, the accuracy could be further improved by defining knockdown factors in order to render conservative predictions.

Appendix A. Condensation of stringer properties

Consider a composite I-beam is used as stiffener on a composite skin, as shown in the figure:
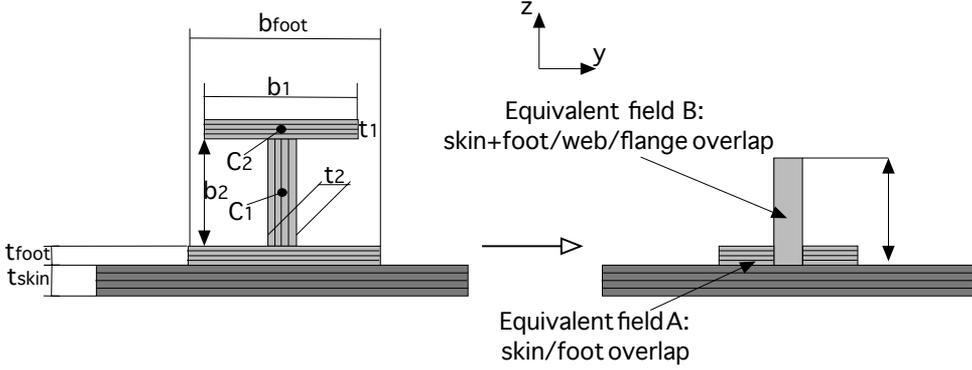
As before, the width of the panel field equals the foot width. We need to assign an equivalent thickness and an equivalent local lamina stiffness matrix $\boldsymbol{Q}^{\mathrm{eq}}$ to the equivalent layer that represents the stiffener. Therefore, we need to properly assess five quantities: the equivalent thickness t_{eq}, the equivalent stiffnesses E_x^{eq} and E_y^{eq} in the x- and y-directions, the equivalent shear modulus G_{xy}^{eq} in the y-direction, and the equivalent Poisson's ratio ν_{xy}^{eq}.

If x is the direction of the main stiffener dimension, E_x^{eq} and t_{eq} are calculated by deriving the global axial (EA_{tot}) and bending (EI_{tot}) of the T-beam formed by the web and upper flange, and then imposing the conditions

$$EA_{\mathrm{tot}} = E_x^{\mathrm{eq}} b_{\mathrm{foot}} t_{\mathrm{eq}}, \qquad EI_{\mathrm{tot}} = E_x^{\mathrm{eq}} \tfrac{1}{12} b_{\mathrm{foot}} t_{\mathrm{eq}}^3. \tag{A.1}$$

The equivalent elastic modulus in the y-direction, orthogonally to the direction of the main stiffener dimension, can be set equal to zero. In fact, it is straightforward to demonstrate that, apart from the lower flange, the remaining part of the stringer does not contribute significantly if in-plane y-loads or transverse y bending moments are applied

$$E_y^{\mathrm{eq}} \cong 0. \tag{A.2}$$

The equivalent shear modulus is calculated as

$$G_{xy}^{\mathrm{eq}} = \frac{1}{b_{\mathrm{foot}} t_{\mathrm{eq}}} \sum_{k=1}^{n_{\mathrm{flanges}}} G_{xy,k} A_k, \tag{A.3}$$

where n_{flanges} is the total number of flanges, $G_{xy,k}$ is the shear modulus of the k-th flange, and A_k is the area of k-th flange.

Note that formula (A.3) neglects the contribution of the vertical webs. Therefore the formula is appropriate if thin walled beams are used as stiffeners. The Poisson's ratios are derived from the assumption that the portion of the stiffener that lies on top of the skin but not directly in contact with it (namely the web and upper flange, see figure) does not affect the effective structural Poisson's ratio when axial loads in x-direction are applied. Hence, the Poisson's ratio ν_{xy}^{eq} equals the Poisson's ratio of the lower flange.

Appendix B. Derivation of the edge loads

To determine the expansion coefficients A_n and B_n, the in-plane unit width loads N_{xi} are assumed to be constant within each subdomain, which may be represented as a spring with a concentrated stiffness. The whole domain is schematized as a system of springs in series and in parallel (Figure A.1, right), which can be reduced to a single equivalent spring constant:

$$k_{\text{eq}} = \frac{k_1(k_2 + k_3 + k_4)}{k_1 + k_2 + k_3 + k_4}. \tag{B.1}$$

The axial flows N_{xi} are calculated throughout the domain under the assumption that every straight line parallel to the y-axis remains straight after the deformation. This assumption does not represent the real strain field throughout the panel's domain. Nonetheless, since only the stress field at the boundary is of interest at this stage, the assumption of discrete variation of N_x is not restrictive if stringer length is sufficiently large. In such a case, the skin-to-stiffener load transfer is already completed far from the boundary, and we can assume that the uniform axial (x-wise) strain condition is reestablished. An example calculation is provided here.

For convenience, we consider a geometry formally identical to the skin-patch composite assembly of Sections 4 and 5. We apply a constant axial flow $N_{x,1}$ on the free edge of the panel (Figure A.1, left). The total force acting is therefore $F_{\text{tot}} = N_{x1}l_y$. The total axial displacement is calculated as

$$\delta_{\text{tot}} = \frac{F_{\text{tot}}}{k_{\text{eq}}}, \tag{B.2}$$

where k_{eq} is as in (B.1), with spring constants given by

$$k_1 = \frac{l_y}{A'_{11,1}} \frac{1}{l_x - l_P}, \qquad k_2 = \frac{l_2}{A'_{11,2}} \frac{1}{l_P}, \qquad k_3 = \frac{l_3}{A'_{11,3}} \frac{1}{l_P}, \qquad k_4 = \frac{l_4}{A'_{11,4}} \frac{1}{l_P}. \tag{B.3}$$

To calculate how the total force distributes into the springs 1, 2, and 3, the axial displacement δ_{234} calculated at $x = l_P$ is first derived; it equals $\delta_{234} = \delta_{\text{tot}} F_1/k_1$, where $F_1 = F_{\text{tot}}$. The force distribution is now given by $F_i = k_i \delta_P$, for $i = 2, 3, 4$. The x-wise axial flows are given by

$$N_{xi} = F_i/l_i.$$
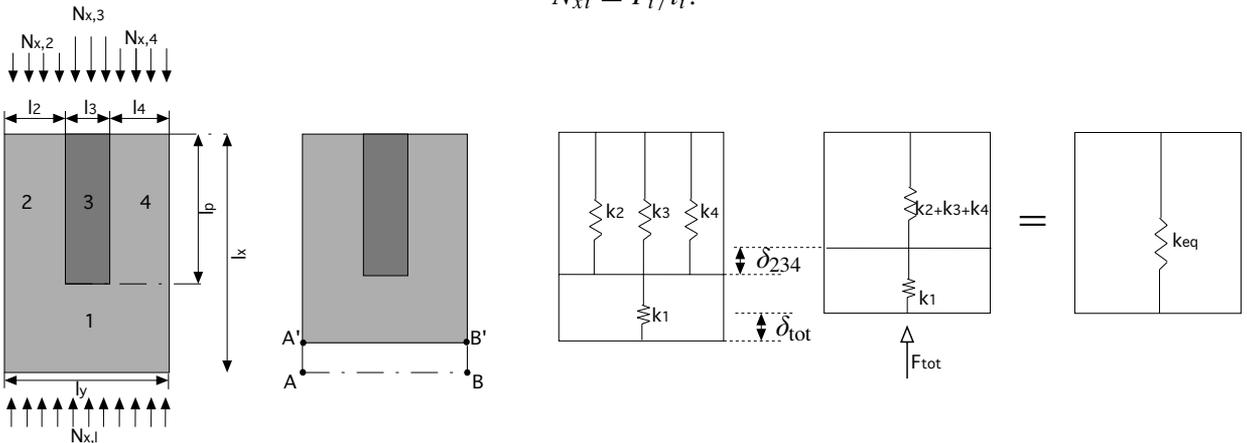
Figure A.1. Domain schematisation and system reduction scheme.

List of symbols

$\boldsymbol{u}_0, \boldsymbol{v}_0$	in-plane displacement of neutral plane in x and y directions
w	out-of-plane displacement
$\varepsilon_x, \varepsilon_y, \varepsilon_{xy}$	in-plane strains
$\varepsilon_x^0, \varepsilon_y^0, \varepsilon_{xy}^0$	in-plane strains at neutral plane level
e	neutral plane function
l_x, l_y	length and width of panel
$\boldsymbol{N}, \boldsymbol{M}$	unit width stresses and bending moments vectors
$\boldsymbol{A}, \boldsymbol{D}$	laminate in-plane and transverse stiffness matrices
$\boldsymbol{B}$	laminate coupling stiffness matrix
Ψ	equilibrium stress function for uniform loading
$\Delta\Psi$	equilibrium stress function for perturbation loading
Ψ_e	equilibrium stress function
Ψ_c	compatibility stress function for perturbation loading
Ω	stress function
$X, Y, \overline{X}, \overline{Y}$	beam eigenfunctions
φ_j	transverse displacement eigenfunctions
$\overline{\varphi}_j$	transverse displacement eigenfunctions
Ψ_j	stress function eigenfunctions
$N_{x,o}, N_{y,o}, N_{xy,o}$	external in-plane loads per unit width
N_x, N_y, N_{xy}	internal in-plane loads per unit width
w_i	generalized coordinates of the displacement function
e_i	generalized coordinates of the neutral plane function
ξ_j	generalized coordinates of the Airy stress function
$\boldsymbol{u}$	generalized coordinates vector
U	internal elastic potential energy
$\Omega_{N,L}$	linear component of the total potential of internal in-plane loads
$\Omega_{N,NL}$	nonlinear component of the total potential of internal in-plane loads
Ω_N	total potential of internal in-plane loads
Π_L	linear component of total potential
Π_{NL}	nonlinear component of total potential
Π	total potential
Ω_Q	potential of external transverse loads
$\boldsymbol{A}^*, \boldsymbol{D}^*$	matrices of in-plane and flexural flexibility in partially inverted laminate constitutive equations
$\boldsymbol{B}^*$	coupling matrix in partially inverted laminate constitutive equations
$\boldsymbol{Q}$	vector defined in (19)
$\boldsymbol{G}, \boldsymbol{H}, \overline{\boldsymbol{H}}$	matrices defined in (21), (22), and (23)
$\Gamma_x, \Gamma_y, \Gamma_{xy}$	circulation functions
ϕ_n	weight functions

Acknowledgments

References

[Ashton et al. 1969] J. E. Ashton, J. C. Halpin, and P. H. Petit, *Primer on composite materials: analysis*, Technomic, Stamford, CT, 1969.

[Cosentino and Weaver 2008] E. Cosentino and P. M. Weaver, "Approximate non linear analysis method for debonding of skin/stringer composite assemblies", *AIAA J.* **46**:5 (2008), 1144–1159.

[Cosentino and Weaver 2009] E. Cosentino and P. M. Weaver, "Nonlinear analytical approach for sizing of discrete composite stringer terminations", *AIAA J.* **47**:3 (2009), 606–617.

[Jaunky et al. 1995] N. Jaunky, N. F. J. Knight, and D. R. Ambur, "Buckling of arbitrary quadrilateral anisotropic plates", *AIAA J.* **33**:5 (May 1995), 938–944.

[Jones 1975] R. M. Jones, *Mechanics of composite materials*, Scripta, Washington, 1975.

[Kollar and Springer 2003] L. P. Kollar and G. S. Springer, *Mechanics of composite structures*, Cambridge University Press, Cambridge, 2003.

[Mansfield 1989] E. H. Mansfield, *The bending and stretching of plates*, 2nd ed., Cambridge University Press, New York, 1989.

[Reddy 2004] J. N. Reddy, *Mechanics of laminated composite plates and shells*, CRC Press, Boca Raton, FL, 2004.

[Timoshenko and Goodier 1982] S. P. Timoshenko and J. N. Goodier, *Theory of elasticity*, 3rd ed., McGraw-Hill, New York, 1982.

[Weaver and Nemeth 2007] P. M. Weaver and P. M. Nemeth, "Bounds on flexural properties and buckling response for symmetrically laminated composite plates", *J. Eng. Mech.* **133**:11 (Nov 2007), 1178–1191.

[Weaver and Nemeth 2008] P. M. Weaver and M. P. Nemeth, "Improved design formulas for buckling of orthotropic plates under combined loading", *AIAA J.* **46**:9 (September 2008).

ENZO COSENTINO: enzo.cosentino@airbus.com
Composite Stress Analysis, Composite Structures Development Centre, Airbus UK Ltd., Bristol BS34 7AR, United Kingdom

PAUL WEAVER: paul.weaver@bristol.ac.uk
Advanced Composite Centre for Innovation and Science, Department of Aerospace Engineering, University of Bristol, Queen's Building 2.39, University Walk, Bristol BS8 1TR, United Kingdom